IEEE Photonics Journal
An IEEE Photonics Society Publication

Open Access

Plasmonic Demultiplexer With Tunable Output Power Ratio Based on Metal-Dielectric-Metal Structure and E7 Liquid Crystal Arrays

Volume 12, Number 3, June 2020

Zelong Wang
Lin Cheng
Yuyao Wu
Chengpu Li
Mingyang Gong
Pengfei Cao
Xiaodong He
Tiaoming Niu

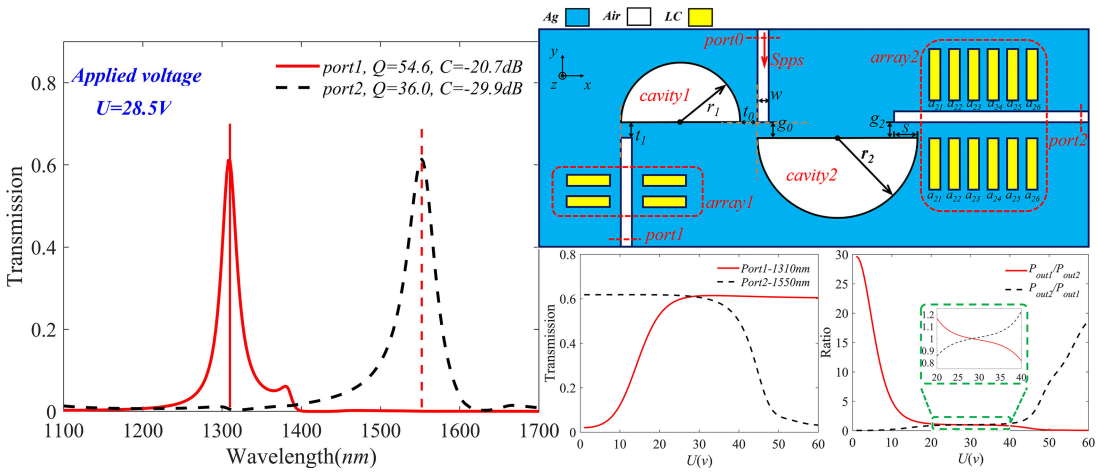

DOI: 10.1109/JPHOT.2020.2987396

Plasmonic Demultiplexer With Tunable Output Power Ratio Based on Metal-Dielectric-Metal Structure and E7 Liquid Crystal Arrays

Zelong Wang, Lin Cheng, Yuyao Wu, Chengpu Li, Mingyang Gong, Pengfei Cao, Xiaodong He, and Tiaoming Niu

Institute of Optoelectronics & Electromagnetic Information, Lanzhou University, Lanzhou 730000, China

DOI:10.1109/JPHOT.2020.2987396

Manuscript received February 26, 2020; revised April 1, 2020; accepted April 8, 2020. Date of publication April 15, 2020; date of current version April 28, 2020. This work was supported in part by the National Natural Science Foundation of China under Grant 61804071 and 61905100, in part by the Natural Science Foundation of Gansu Province under Grant 1606RJZA068 and 18JR3RA297, and in part by the Fundamental Research Funds for Central Universities (lzujbky-2020-65). Corresponding author: Lin Cheng (e-mail: chenglin@lzu.edu.cn).

Abstract: A novel tunable plasmonic demultiplexer is proposed and numerically investigated by finite element method (FEM). It consists of two half-nanodisk cavities and two sets of E7 liquid crystal arrays which are side-coupled to three metal-dielectric-metal (MDM) waveguides. The demultiplexer can split the input lights into two parts corresponding to port1 (1310 nm) and port2 (1550 nm). The Q-factors of port1 and port2 are 54.6 and 36, and the crosstalk values are −20.7 dB and −29.9 dB, respectively. Obviously, both channels have high Q-factors and low crosstalk value. Moreover, the E7 liquid crystal arrays play a key role in the whole structure, which makes the output power adjustable proportionally by adjusting the applied voltage. This novel feature greatly enriches the function of our demultiplexer. Using the electronical tunable birefringence characteristic of liquid crystal and its arrays structure paves a new way to realize practical on-chip plasmonic system, which can be widely used not only in demultiplexers but also in nanosensors, optical splitters, filters, optical switches, nonlinear photonic and slow-light devices.

Index Terms: Metal-dielectric-metal (MDM) waveguide, surface plasmon polaritons (SPPs), demultiplexer, on-chip plasmonic system.

1. Introduction

Surface plasmon polaritons (SPPs) excited at the interface between metal and dielectric have bigger propagation constant and smaller wavelength at the same frequency. Therefore, SPPs can break the classical diffraction limit of light [1]. Among the commonly ways to excite SPPs, such as prism excitation [2], grating excitation [3], waveguide coupling excitation [4] and near-field excitation [5], the metal-dielectric-metal (MDM) waveguide structure is more suitable for highly integrated optical circuits due to its compact size and easy integration [6]. The MDM structure can confine the optical field locally and propagate SPPs along the waveguide with a corresponding low power loss, thus the MDM structures have become one of hotspot in optical field, a series of high performance devices, such as refractive index sensors [7]–[9], optical switches [10], [11], optical filters [12], [13],

and demultiplexers [14], [15], have been reported in the last few years. Demultiplexer, as one of the important devices in on-chip system, has been widely studied recently. There are two common coupling types in MDM demultiplexers – one is that the resonators are directly side-coupled to one bus waveguide between the input and output ports [16], the other is that the input waveguide, output waveguide and resonators are all coupled through a gap [14], [15], [17]. In recent years, more and more demultiplexers with better performance are reported [6], [14], [18]. Among them, the closest one to our wavelength range is reference [6], whose classic performance parameter is $C = -9.05$ dB, $Q = 15.6$ for 1310 nm and $C = -15.49$ dB, $Q = 21$ for 1550 nm. However, they all tend to have the same defect that the output power of each port only varies with the input power, and the output power ratio between each output port cannot adjust. Obviously, the demultiplexer without tunable output power ratio is disadvantage to the practical application with consuming more intermediate devices.

In the current status, as to our knowledge, researches about demultiplexers on these issues have not gone far enough. Hence, aiming at the issues, we added E7 liquid crystal in the traditional MDM structure to make the whole structure tunable by applied voltage. Liquid crystal (LC) is a feasible option to manipulate SPPs on a subwavelength scale, because the tilt angle of its optical axis can be controlled by applied voltage [19]. In the past few years, due to its electronic birefringence and low power consumption in near infrared region (NIR), LC is widely used in modulation devices such as optofluidic filter [20] and polarization rotator [21].

In this paper, we designed an electrically tunable plasmonic demultiplexer, which consists of a demultiplexing part and an output power modulation part. The demultiplexing part is composed of an input waveguide and two half-nanodisk resonators. And the output power modulation part is made up of two vertical output waveguides, each of which side-coupled an array of E7 liquid crystal. The transmission spectra of the whole system are numerically simulated by finite element method (FEM). The simulation results show that each output port has a narrow resonance peak with a transmissivity nearly equal to 0.61 corresponding to 1310 nm for port1 and 1550 nm for port2 when applied voltage is 28.5 V, and the Q factor and crosstalk values for each output port are 54.6 and -20.7 dB, 36 and -29.9 dB, respectively. Moreover, the modulation properties of E7 liquid crystal arrays are further investigated in details. By adjusting the applied voltage from 1 V to 60 V, it can be specified any output power ratio through these two output ports. This is attributed to the elaborate design that the alignment orientation of the two sets of E7 liquid crystal arrays is perpendicular. Compared with similar reported demultiplexers [6], [14], our structure has better performance and richer features with flexibility. Thus, our structure is potential for on-chip demultiplexers with high performance. Moreover, our study on the characteristics of liquid crystal arrays also provides a powerful theoretical guidance for all-optical integration systems and ultra-compact plasmonic devices.

2. The Basic Demultiplexer Structure

Fig. 1 shows the schematic diagram of our basic demultiplexer, which consists of three straight waveguides and two half-nanodisk resonators (denoted as *cavity1* and *cavity2*). For convenience, the input port is denoted as *port0*, the two output ports (1310 nm, 1550 nm) are named as *port1* and *port2*, respectively. In this paper, the width of three straight waveguides are fixed at $w = 50$ nm. r_1 and r_2 are the radius of *cavity1* and *cavity2*, respectively. t_0 (g_0), t_1(g_2) are the coupled gap of *cavity1* (*cavity2*) to *port0* and *port1* (*port2*), respectively. S is the length of the overlap between the *cavity2* and *port2*. It can be seen in Fig. 1 that only air and silver are filled in the structure corresponding to white and blue areas, respectively. In this paper, we set the relative permittivity of air to $\varepsilon_d = 1$, and the relative permittivity of silver described by the Drude-model covering the wavelength range of $1100 \sim 1700$ nm, which represent by [22]

$$\varepsilon_m(\omega) = \varepsilon_\infty - \omega_p^2 / \left(\omega^2 + i\omega\gamma_p\right) \tag{1}$$

where $\varepsilon_\infty = 3.7$ is the electric constant at the infinite angular frequency, the bulk plasma frequency $\omega_p = 1.38 \times 10^{16}$ rad/s, the damping rate $\gamma_p = 2.73 \times 10^{13}$ rad/s characters the absorption loss,

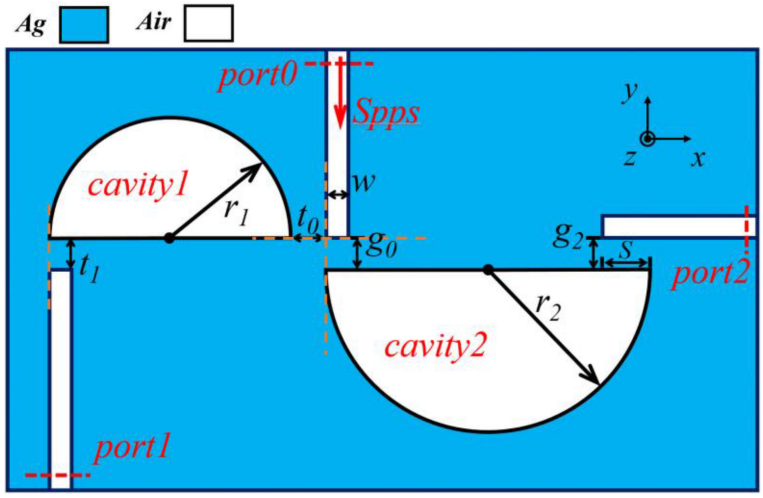

Fig. 1. Schematic diagram of the origin demultiplexer.

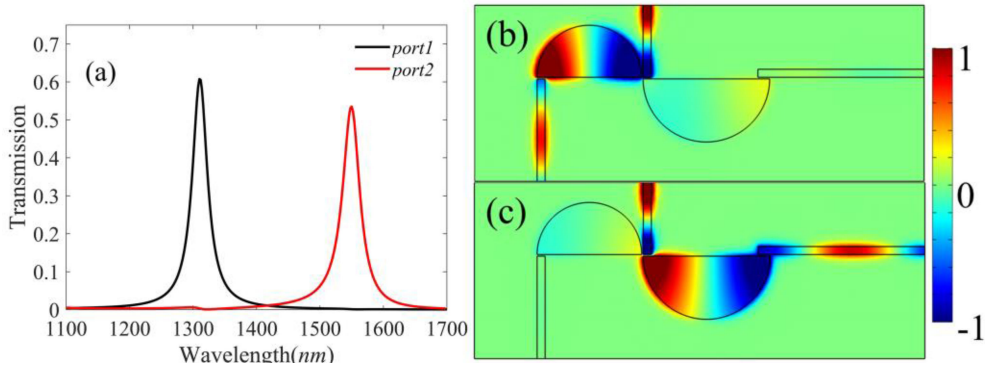

Fig. 2. (a) Transmission spectra of the basic demutiplexer. The *Hz* field of the resonance wavelength at 1310 nm (b) and 1550 nm (c).

and ω is the angle frequency of incident light. A *TM* polarized plane wave is launched and excited the SPPs to *port0*. Here P_{in} and P_{out1}, P_{out2} stand for input and output power flows of *port0*, *port1* and *port2*, respectively. Then the transmission of the structure can be defined as $T_i = \frac{P_{outi}}{P_{in}}$, $(i = 1, 2)$.

The basic structure of our demultiplexer, as shown in Fig. 1, is numerically investigated by using the finite element method (FEM), also comparative by the classical coupled modes theory (CMT). In order to explore the properties of the demultiplexer further, we performed a series of numerical simulations to discuss the mechanism of our design. Firstly, the basic demultiplexer was investigated in detail and the transmission spectra are shown in Fig. 2(a). The geometric dimensions of the structure are as follows, $r_1 = 325$ nm, $r_2 = 394$ nm, $t_0 = t_1 = g_0 = g_2 = 10$ nm, $S = 73$ nm.

The black solid line in Fig. 2(a) shows a resonance peak with a value of 0.61 at 1310 nm, while the red solid line shows another resonance peak with a value of 0.54 at 1550 nm. To reveal the mechanism of these two resonance modes, we plotted the z-component of the magnetic field intensity (H_z) at 1310 nm and 1550 nm and the results are shown in Fig. 2(b) and (c), respectively. As shown in Fig. 2(b), the magnetic energy is concentrated in the *cavity1*, the SPPs wavelength meets the stand-wave condition of *cavity1*, so that the SPPs wave can be coupled to the *port1* to form a transmission peak. A similar situation occurs in the right half of the disk and in *port2* the wavelength of 1550 nm has been selected, as shown in Fig. 2(c). It means that the compound multiplexing modes can be demultiplexed as two independent ones by this MDM structure.

For purpose to verify the reliability of the simulation results, we also analyze our structure by coupled mode theory (CMT) [23], [24]. The coupling-of-modes formalism is general and can be applied to numerous physical systems possessing resonant modes. In terms of our structure, there are mainly two modes excited by the resonators and output waveguides, and the high-order modes of each resonator are out of the wavelength range we discussed. Since the high-order modes is very small, we ignore the interference effect from the high-order modes. Therefore, we can investigate the demultiplexer in these two modes separately, each of which can be seen as a resonator is connected to two waveguides for each mode, and the equations can be expressed as follows

$$\frac{da_m}{dt} = -j\omega_m a_m - \left(\frac{1}{\tau_{m0}} + \frac{1}{\tau_{m1}} + \frac{1}{\tau_{m2}}\right) a_m + \kappa_{m1} S_{\mathrm{m1}+} + \kappa_{m2} S_{\mathrm{m2}+} \tag{2}$$

$$S_{\mathrm{m1}-} = -S_{\mathrm{m1}+} + \kappa_{m1}^* a_m \qquad \kappa_{m1} = \sqrt{\frac{2}{\tau_{m1}}} e^{j\theta_{m1}} \tag{3}$$

$$S_{\mathrm{m2}-} = -S_{\mathrm{m2}+} + \kappa_{m2}^* a_m \quad , \quad \kappa_{m2} = \sqrt{\frac{2}{\tau_{m2}}} e^{j\theta_{m2}} \tag{4}$$

Where $m = 1,\ 2$ represent the modes with the resonance wavelength of 1310 nm and 1550 nm for *port1* and *port2*, respectively. a_m and ω_m are the field amplitude and resonant frequency of the *m*th mode, respectively. τ_{m0} is the decay time of internal loss of the mth mode in the resonant system. τ_{m1}, τ_{m2} are the decay time of the coupling between the resonator and input, output waveguides, respectively. κ_{m1} and κ_{m2} are the coupling coefficient between the resonant system and the input, output waveguides, respectively. θ_{m1} and θ_{m2} are the complex amplitude phases of the *m*th resonant mode coupled to the input, output waveguides. $S_{mi\pm}$ are the field amplitudes in each mode ($m = 1,\ 2$) and *port1* or *port2* (*i= 1, 2*) for outgoing ($-$) or incoming ($+$) from the resonator. In this paper, only *port0* has *TM* wave incidence. Hence, $S_{\mathrm{m2}+} = 0$, and the transmission T_m is satisfied the following equation

$$T_m = |t_m|^2 = \left|\frac{S_{\mathrm{m2}-}}{S_{\mathrm{m1}+}}\right|^2 = \left|\frac{2e^{j\varphi_m}}{-j\left(\omega - \omega_m\right)\sqrt{\tau_{m1}\tau_{m2}} + \frac{\sqrt{\tau_{m1}\tau_{m2}}}{\tau_{m0}} + \sqrt{\frac{\tau_{m1}}{\tau_{m2}}} + \sqrt{\frac{\tau_{m2}}{\tau_{m1}}}}\right|^2 \quad , \quad \varphi_m = \theta_{m1} + \varphi_{m0} - \theta_{m2} \tag{5}$$

Where t is the transmission coefficient and φ_{m0} is the internal phase difference of the *m*th resonant mode. φ_m is the total coupling phase difference of the *m*th resonant mode. As in our design, through the analysis of the simulation results, we can obtain $\varphi_1 = 0.53\pi$ and $\varphi_2 = 0.24\pi$, respectively.

Then, we used CMT and the results of the numerical simulation for curve fitting and obtained the transmission spectra for *port1* and *port2* in Fig. 3(a) and (b), respectively. It can be seen that both curves have good fitting results, which confirmed further that it is reasonable to ignore the influence of the higher order modes in the half-nanodisk resonators.

The performance of demultiplexer is commonly judged by quality factor and crosstalk. As we know, the Q-factor is the measure of energy stored in the resonator and is given as $Q = \lambda_0/FWHM$, where λ_0 is the resonant wavelength and FWHM is full width at half maximum. The values of the Q-factor are *45.2* and *47* for *port1* (1310 nm) and *port2* (1550 nm), respectively. While crosstalk is defined as [25]: $C = 10\ log\ (\frac{P_{op}}{P_{ip}})$, which represents the ability of the device to separate different signals. The lower the crosstalk value, the stronger ability to separate signals and the smaller interference between different signals. Here, P_{ip} is the power of interested port and P_{op} is the power of the other port. The crosstalk value of our basic demultiplexer is -22.4 dB for *port1* and -26.4 dB for *port2*, respectively. Compared with similar devices [6], [14], the performance of our demultiplexer is much better.

But from our point of view, there's still a defect cannot be ignored that the output power of the two ports are not equal and the output power ratio cannot be regulated. Because the resonance

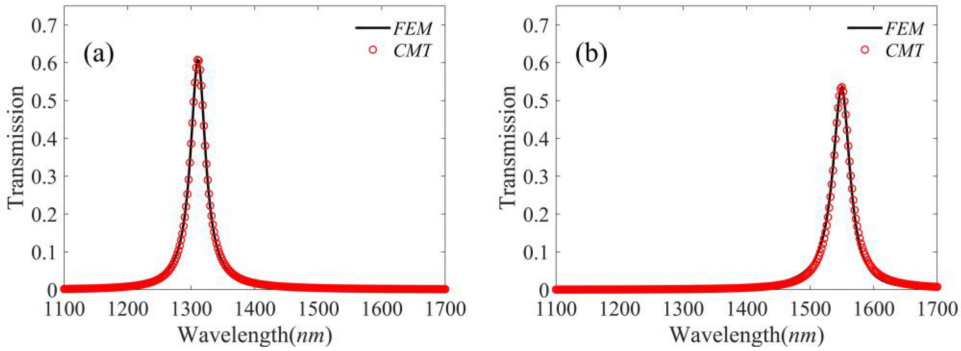

Fig. 3. Curve fitting results for *port1*(a) and *port2*(b). The CMT parameters can be obtained by curve fitting that the decay time of internal loss $\tau_{10} = 513fs$ and $\tau_{20} = 348fs$, the decay time of the coupling between the resonator and waveguides $\tau_{11} = 100fs$, $\tau_{12} = 266fs$, $\tau_{21} = 310fs$, and $\tau_{22} = 152fs$.

of basic structure depends on the property of material and the dimension. When the structure is made, the peak position and amplitude of the resonance is determined. This phenomenon limits the basic demultiplexer in the practical application. An additional power modulation part needs to be considered to make the whole system more flexible. Aiming at this issue, we further optimized our demultiplexer by utilizing electrical-tuned materials. In the following part, we will discuss the specific properties of E7 liquid crystals and the principles used in the optimization process in detail.

3. The Optimized Structure by Utilizing E7 Liquid Crystals Arrays

As we know, E7 liquid crystal is an anisotropic uniaxial crystal. Its extraordinary refractive index (n_e) and ordinary refractive index (n_o) are expressed as following Cauchy equations

$$n_e = A_e + \frac{B_e}{\lambda^2} + \frac{C_e}{\lambda^4} \tag{6a}$$

$$n_o = A_o + \frac{B_o}{\lambda^2} + \frac{C_o}{\lambda^4} \tag{6b}$$

Where A_e, B_e, C_e, A_o, B_o and C_o are six Cauchy coefficients. All these Cauchy coefficients can be obtained by fitting the experimental results. The fitting results of these six parameters at 20 °C are 1.6993, 0.0085, 0.0027, 1.4998, 0.0067 and 0.0004, respectively [26].

Given the optical axes of all liquid crystal molecules are along the x-axis without any excitation. When an electric field is applied in the direction of the y-axis, all molecules are assumed to tilt by an angle θ tending to align with the applied electric field. The function between the voltage U and the tilt angle θ is expressed by the following equation

$$\theta = \begin{cases} 0 & , U \le V_{th} \\ \frac{\pi}{2} - 2tan^{-1}\left\{exp\left[-\left(\frac{U-V_{th}}{V_0}\right)\right]\right\} & , U > V_{th} \end{cases} \tag{7}$$

where U is the applied voltage, V_0 is a classic voltage at which the tilt angle is 49.6° [27]. And $V_{th} = \pi\sqrt{\frac{K_{11}}{\Delta\varepsilon\varepsilon_0}}$ is the threshold voltage, below which no tilting will occur [28]. K_{11} is the splay elastic constant of liquid crystal, $\varepsilon_0 = 8.85\ pF/m$ is the electric constant in free space and $\Delta\varepsilon = \varepsilon_{\parallel} - \varepsilon_{\perp}$ is the anisotropy dielectric permittivity, where $\varepsilon_{\parallel}$ and $\varepsilon_{\perp}$ are the parallel and perpendicular components of the electric permittivity of E7 liquid crystals. The value of K_{11}, $\varepsilon_{\parallel}$ and $\varepsilon_{\perp}$at 20 °C can be found in the reference [29]. For $U > V_{th}$(0.95 V, 20 °C), the tilt angle θ increases with the increase of U.

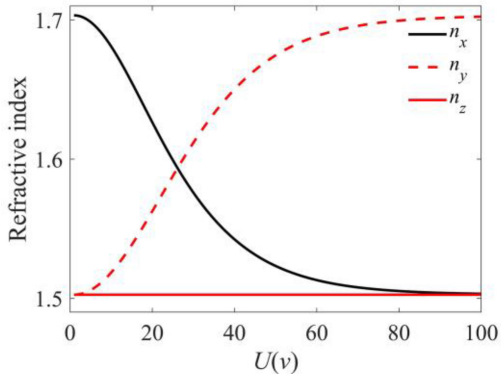

Fig. 4. The relationship between refractive index components and the applied voltage U

According to the birefringence ellipsoid of E7 liquid crystals, the component of the refractive index along incident light with the tilt angle θ to the optical axis in the liquid crystal can be expressed by

$$n = \left(\frac{sin^2\theta}{n_e^2} + \frac{cos^2\theta}{n_o^2} \right)^{-\frac{1}{2}} \tag{8}$$

In this paper, we set the default orientation of the liquid crystal optical axis along the x-axis, and the direction of the applied voltage is along the y-axis. Then according to the index ellipsoid of a uniaxial crystal and Equations(6-8), we can plot the dependence of the three-component (x, y and z) of the refractive index of E7 liquid crystal and the applied voltage U, as shown in Fig. 4. It can be seen that as the voltage increases, n_x decreases gradually and approaches n_o, n_y increases gradually, reaching a saturation value of n_e, and n_z remains stable which is always equal to n_o.

Next, we discussed the transmission properties of the side-coupled arrays. In this paper, we selected paired rectangular bars to fill the E7 liquid crystal, which are double side-coupling the straight output waveguides. The features of the bar arrays are investigated in the following part. Each bar can be regarded as a rectangular resonator, and the standing wave conditions are expressed as follows

$$\lambda_{res} = \frac{2n_{eff}L_{eff}}{m - \varphi_r/\pi}, m = 1, 2, 3 \ldots, \tag{9}$$

where n_{eff} is the effective refractive index in the resonator, and L_{eff} is the effective length of the cavity. m is a positive integer, which represents the order of the resonate mode. φ_r is the phase shift of SPPs reflected on the facets of the cavity.

$$\varepsilon_m \sqrt{\beta_{spp}^2 - \varepsilon_d k_0^2} tanh\left(\frac{w\sqrt{\beta_{spp}^2 - \varepsilon_d k_0^2}}{2} \right) + \varepsilon_d \sqrt{\beta_{spp}^2 - \varepsilon_m k_0^2} = 0 \tag{10}$$

where $\beta_{spp} = k_0 n_{eff}$ is the propagation constant of the SPPs in the resonator, $k_0 = 2\pi/\lambda$ is free space wavenumbers. ε_m and ε_d are the relative permittivity of metal and dielectric, respectively.

Fig. 5(a) shows the schematic diagram of the E7 liquid crystal arrays. The length, the width of each rectangular bar and the refractive index of E7 liquid crystal are set to be $l = 230$ nm, $w = 50$ nm *and* $n_0 = 1.5$, respectively. The resonance wavelength of the structure can be controlled at around 1310 nm, which is a convenient and traditional optical window. The dependence between the resonance wavelength and the size of the bar can be derived from Equations (9, 10), and the details of which have been discussed in our previous work [30]. The distance between adjacent bars in the array is fixed at $D = 100$ nm, avoiding the adjacent bar interference while maintaining a compact size for integration. Afterwards, we investigated two important parameters: (i) the number of the bar periods (N), (ii) the side-coupled gap (d) between the output port and the arrays. The results are shown in Fig. 5(b) and (c).

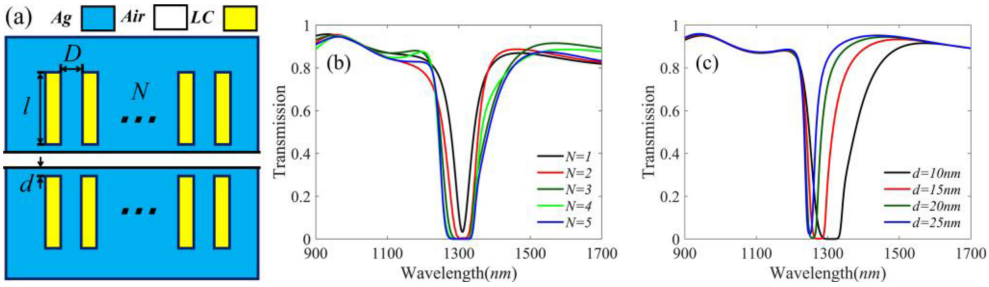

Fig. 5. (a) Schematic diagram of the E7 liquid crystal arrays. Transmission spectra of different parameters, (b) the number of the arrays period(*N*), (c) the side-coupled gap between output port, and the arrays(*d*).

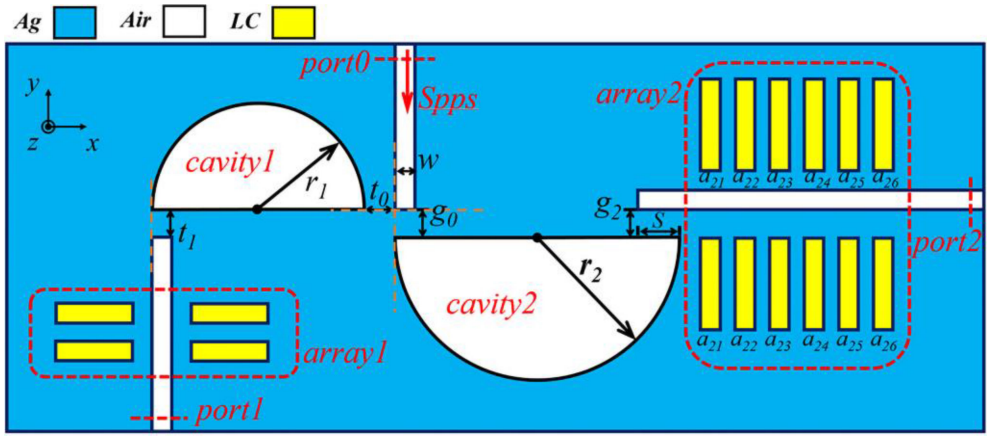

Fig. 6. Schematic diagram of the optimized demultiplexer.

Fig. 5(b) shows the transmission spectra of different *N*. It can be seen there is a bandgap between 1200 $\sim$ 1400 nm. With the increase of *N*, the width of bandgap will increase with a decreasing growth rate, and the transmission of the structure decreases. This can be attributed to that each bar produces a superposition effect of the transmission dip in the same region. After that, we set $N = 3$ to discuss the effect of coupling gap(*d*) on the transmission spectra, as shown in Fig. 5(c). With the increase of *d*, the coupling effect between the array and the waveguide is reduced, thus the position of the resonance wavelength has a blue shift, the width of bandgap gradually narrowed, and the transmission gradually increased. It is worth noting that by setting the appropriate parameters above, we can obtain a suitable band-stop filter transmission line shape with a steep transition band, an appropriate stopband bandwidth, and a relatively flat passband adjacent to the transition band. This design concept can also guide the design of band-stop filters.

By utilizing the electronic birefringence characteristic of the E7 liquid crystal (Fig. 4) and the band stop features of the double side-coupled rectangular bar array (Fig. 5), we developed the basic original demultiplexer into a complex one, as shown in Fig. 6. That is the output power can be adjusted proportionally by controlled the applied voltage on E7 liquid crystal arrays.

The introduction of the liquid crystal arrays in each output port will also have a slight impact on the basic original demultiplexer. After optimization, the width of all the rectangular bars is 50 nm. The period number(*N*) of the bar arrays for *port1* and *port2*, denoted as *array1* and *array2*, are 2 and 6, respectively. The distance between adjacent bars in both arrays are fixed at $D = 100$ nm. The coupled gap of *array1* and *array2* are 10 nm and 15 nm, respectively. The length of each bar in *array1* is $l_{\mathrm{a1}} = 271$ nm, and in *array2* is as follows: $l_{\mathrm{a21}} = 334$ nm, $l_{\mathrm{a22}} = 336$ nm, $l_{\mathrm{a23}} = l_{\mathrm{a24}} = 338$ nm, $l_{\mathrm{a25}} = 340$ nm and $l_{\mathrm{a26}} = 342$ nm. Besides, in the optimized demultiplexer shown in Fig. 6,

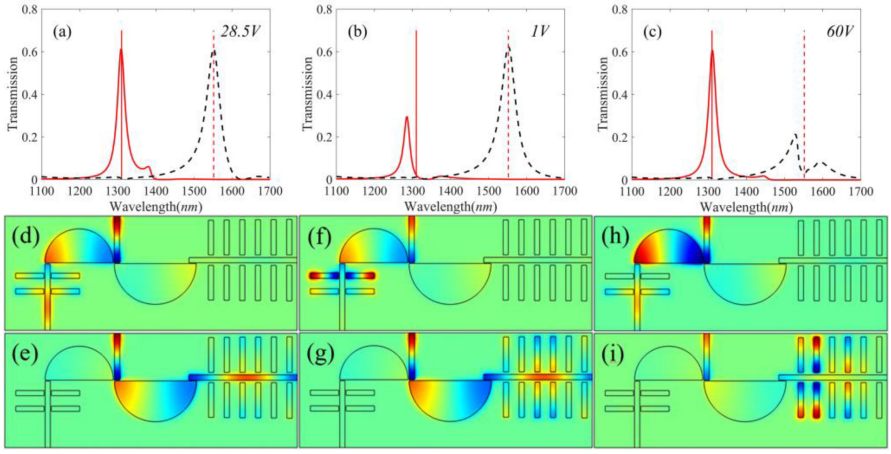

Fig. 7. Transmission spectra of the final structure when the applied voltage at three classic value (a) 28.5 V, (b) 1 V, and (c) 60 V. The Hz field at 1310 nm and 1550 nm when the applied voltage at 28.5 V (d, e), 1 V (f, g), and 60 V (h, i), respectively.

the original parameters have changed to $r_1 = 326$ nm, $r_2 = 392$ nm, $t_0 = 12$ nm, $t_1 = 10$ nm, $g_0 = g_2 = 8$ nm, $S = 69$ nm. All the slight size tuning is intended to achieve a better proportional output power performance.

As an example, we have realized a low/high level applied voltage controlled 1×2 demultiplexer, the transmission spectra of the final structure are shown in Fig. 7(a), (b) and (c). The two output ports have three typical cases: (i) both *port1* (1310 nm) and *port2*(1550 nm) passing simultaneously ($U = 28.5$ V), (ii)only *port1* (1310 nm) passing ($U = 1$ V), and (iii) only *port2* (1550 nm) passing ($U = 60$ V), respectively. When the applied voltage is 28.5 V, the transmission of both output ports are 0.61, the output power ratio is almost 1:1. When the applied voltage is 1 V, the transmission of the two ports are 0.02 and 0.61, The output power ratio is almost 1:30. When the applied voltage is 60 V, the transmission of the two ports are 0.61 and 0.03, the output power ratio is almost 20:1. Fig. 7(d) and (e) show the magnetic field s(H_z) at the applied voltage of 28.5 V. Due to both wavelengths do not meet the resonance conditions of E7 liquid crystals arrays, it can be seen that the magnetic field distribution is similar to that in Fig. 2(b) and (c), only a small amount of energy is coupled into the liquid crystal array. Fig. 7(f) and g show the H_z distribution when the applied voltage is 1 V. In Fig. 7(f), most of the energy coupled from *cavity1* to the output waveguide is coupled to *array1*, thus the transmission of *port1* is almost be *0*, however, the SPPs waves from *cavity2* do not meet the resonance conditions of *array2*, as shown in Fig. 7(g) so the transmission of *port2* remains 0.61. When the applied voltage is 60 V, the opposite situations are shown in Fig. 7(h) and (i).

When tuning the applied voltage, we can control the refractive index of the liquid crystal array continuously. The n_{eff} of *array1* increases with the increase of the applied voltage, while the n_{eff} in *array2* decreases, because the alignment orientation of these two arrays are perpendicular. By adjusting the refractive index of *array1* and *array2*, the position of the transition band of these two arrays(as band-stop filters) can be adjusted elaborately, thus the transmission of *port1* and *port2* is changed smoothly.

Fig. 8(a) shows the dependence of the transmission of the two ports in their resonance wavelength (1310 nm for *port1*, 1550 nm for *port2*) and the applied voltage, respectively. The red solid line in Fig. 8(a) shows the transmission spectrum of *port1*. It can be seen that with the increase of applied voltage, the transmission gradually increases from the minimum value about 0.02 to the maximum value about 0.61 when the applied voltage from 1 V to 28.5 V, while the transmission change of *port2* is less than 0.01 (i.e., 1310 nm in the transition band of *array1*, 1550 nm in the flat pass band of *array2*). And after that, when the applied voltage range is 28.5–60 V, the symmetrical

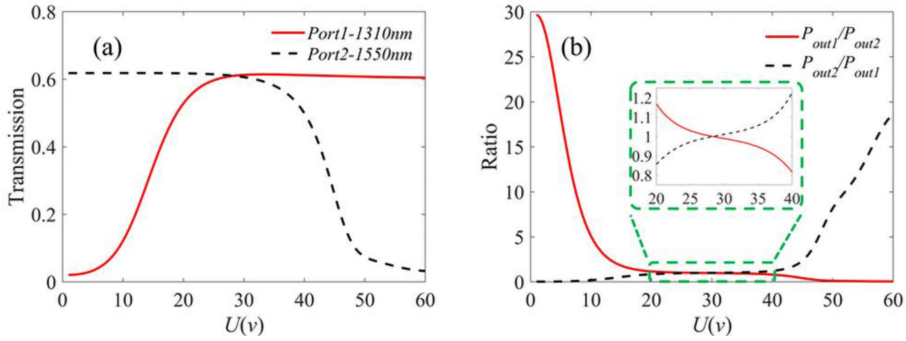

Fig. 8. (a) The dependence of the transmission of *port1* (1310 nm, red line) and *port2* (1550 nm, black line) and the applied voltages (*U*), (b) the dependence of the output power ratio and the applied voltages (*U*).

transmission spectra are shown, as the red and black lines are interchanged (i.e., 1310 nm in the flat pass band of *array1*, 1550 nm in the transition band of *array2*). Fig. 8(b) shows the dependence of the output power ratio and the applied voltages(*U*), as the applied voltage gradually increases from 1 V to 20 V, the red solid line shows that $P_{\mathrm{out1}}/P_{\mathrm{out2}}$ has a steep monotonic descent, while $P_{\mathrm{out2}}/P_{\mathrm{out1}}$ has a steep monotonic increase when *U* increase from 40 V to 60 V. Around 28.5 V is the segment where the ratio is close to 1:1.

When the output power is equal in both output ports (i.e., the applied voltage is 28.5 V), the Q-factor and the crosstalk of the optimized structure for *port1* and *port2* are 54.6 and -20.7 dB, 36 and -29.9 dB, respectively. In addition, the ratio of the output power can be continuously tuned by regulating the applied voltage conveniently. Hence, the structure has pretty good performance compared with the existing demultiplexer. The analysis about the side-coupled resonator arrays can provide a theoretical guidance for filters design. This demultiplexer, as a kind of MDM structure, can be considered as a suitable part for the photonic integrated circuits. Thus, the device can find its application in all-optical, high speed and large information carrying and processing systems.

4. Conclusions

In summary, we report a novel demultiplexer which is composed of two half-nanodisks and two sets of E7 liquid crystal arrays side-coupled with three MDM waveguides. It contains one input port and two output port corresponding to two fundamental optical windows (i.e., 1310 nm and 1550 nm). The transmission spectra of whole system are numerically analyzed by finite element method (FEM). The simulation results show that the transmission of each peak is almost equal to 0.61 when applied voltage is 28.5 V. After that, we investigate the influence of changing voltage on transmission response, and the results show that the output power of the two ports could be adjusted proportionally when the applied voltage varies from 1 V to 60 V. Compared with similar devices, the greater Q-factor, the lower crosstalk value and the adjustable output power ratio are the most outstanding advantages of our demultiplexer. The analysis of electronic control performance of E7 liquid crystal array in this paper will provide a powerful theoretical guidance for future plasmonic device design. In addition, our structure may have important potential applications for compact on-chip plasmonic systems.

References

[1] W. L. Barnes, A. Dereux, and T. W. Ebbesen, "Surface plasmon subwavelength optics," *Nature*, vol. 424, no. 6950, pp. 824–830, 2003.
[2] A. Otto, "Excitation of nonradiative surface plasma waves in silver by the method of frustrated total reflection," *Zeitschrift für Physik A Hadrons Nuclei*, vol. 216, no. 4, pp. 398–410, 1968.

[3] J. W. Cleary, G. Medhi, R. E. Peale and W. R. Buchwald, "Long-wave infrared surface plasmon grating coupler," *Appl. Opt.*, vol. 49, no. 16, pp. 3102–3110, 2010.
[4] Y. Matsuzaki, T. Okamoto, M. Haraguchi, M. Fukui, and M. Nakagaki, "Characteristics of gap plasmon waveguide with stub structures," *Opt. Express*, vol. 16, no. 21, pp. 16314–16325, 2008.
[5] B. Hecht, H. Bielefeldt, L. Novotny, Y. Inouye, and D. W. Pohl, "Local excitation, scattering, and interference of surface plasmons," *Phys. Rev. Lett.*, vol. 77, no. 9, pp. 1889–1892, 1996.
[6] R. Zafar, P. Chauhan, M. Salim, and G. Singh, "Metallic slit–loaded ring resonator–based plasmonic demultiplexer with large crosstalk," *Plasmonics*, vol. 14, no. 4, pp. 1013–1017, 2018.
[7] S. Li, Y. Zhang, X. Song, Y. Wang, and L. Yu, "Tunable triple Fano resonances based on multimode interference in coupled plasmonic resonator system," *Opt. Express*, vol. 24, no. 14, pp. 15351–15361, 2016.
[8] J. Qi *et al.*, "Independently tunable double Fano resonances in asymmetric MIM waveguide structure," *Opt. Express*, vol. 22, no. 12, pp. 14688–14695, 2014.
[9] H. Lu, X. Liu, D. Mao, and G. Wang, "Plasmonic nanosensor based on Fano resonance in waveguide-coupled resonators," *Opt. Lett.*, vol. 37, no. 18, pp. 3780–3782, 2012.
[10] S. Paul and M. Ray, "Multispectral switching using fano resonance and plasmon-induced transparency in a plasmonic waveguide-coupled resonator system," *Plasmonics*, vol. 14, no. 5, pp. 1113–1122, 2019.
[11] F. Chen and D. Yao, "Tunable multiple all-optical switch based on multi-nanoresonator-coupled waveguide systems containing Kerr material," *Opt. Commun.*, vol. 312, pp. 143–147, 2014.
[12] H. Wang *et al.*, "Tunable band-stop plasmonic waveguide filter with symmetrical multiple-teeth-shaped structure," *Opt. Lett.*, vol. 41, no. 6, pp. 1233–1236, 2016.
[13] G. Zhan, R. Liang, H. Liang, J. Luo, and R. Zhao, "Asymmetric band-pass plasmonic nanodisk filter with mode inhibition and spectrally splitting capabilities," *Opt. Express*, vol. 22, no. 8, pp. 9912–9919, 2014.
[14] Z. Zhang *et al.*, "Plasmonic filter and demultiplexer based on square ring resonator," *Appl. Sci.*, vol. 8, no. 3, Mar. 2018, Art. no. 462.
[15] G. Wang, H. Lu, X. Liu, D. Mao, and L. Duan, "Tunable multi-channel wavelength demultiplexer based on MIM plasmonic nanodisk resonators at telecommunication regime," *Opt. Express*, vol. 19, no. 4, pp. 3513–3518, 2011.
[16] Y.-Y. Xie, C. He, J.-C. Li, T.-T. Song, Z.-D. Zhang, and Q.-R. Mao, "Theoretical investigation of a plasmonic demultiplexer in MIM waveguide crossing with multiple side-coupled hexagonal resonators," *IEEE Photon. J.*, vol. 8, no. 5, Oct. 2016, Art. no. 4802512.
[17] J. Chen, Z. Li, J. Li, and Q. Gong, "Compact and high-resolution plasmonic wavelength demultiplexers based on Fano interference," *Opt. Express*, vol. 19, no. 10, pp. 9976–9985, 2011.
[18] X.-S. Li, N. Feng, Y.-M. Xu, L.-L. Cheng, and Q. Liu, "Design of a liquid-crystal-tunable terahertz demultiplexer based on a metal-insulator-metal waveguide," *Appl. Sci.*, vol. 9, no. 4, Feb. 2019, Art. no. 644.
[19] D. H. Lee and M. H. Lee, "Gapped surface plasmon polariton waveguide device based on a liquid crystal," *J. Nanoscience Nanotechnology*, vol. 15, no. 10, pp. 7711–7716, 2015.
[20] F. Chen and D. Yao, "Optofluidic tunable plasmonic filter based on liquid-crystal microcavity structures," *J. Modern Opt.*, vol. 61, no. 18, pp. 1486–1491, 2014.
[21] M. F. O. Hameed, F. F. K. Hussain, and S. S. A. Obayya, "Ultracompact polarization rotator based on liquid crystal channel on silicon," *J. Lightw. Technol.*, vol. 35, no. 11, pp. 2190–2199, Jun. 2017.
[22] Z. Han and S. I. Bozhevolnyi, "Plasmon-induced transparency with detuned ultracompact Fabry-Perot resonators in integrated plasmonic devices," *Opt. Express*, vol. 19, no. 4, pp. 3251–3257, 2011.
[23] W. P. Huang and J. Mu, "Complex coupled-mode theory for optical waveguides," *Opt. Express*, vol. 17, no. 21, pp. 19134–19152, 2009.
[24] J. Mu and W. P. Huang, "Complex coupled-mode theory for tapered optical waveguides," *Opt. Lett.*, vol. 36, no. 6, pp. 1026–1028, 2011.
[25] K. Nakayama, Y. Tonooka, M. Ota, Y. Ishii, and M. Fukuda, "Passive plasmonic demultiplexers using multimode interference," *J. Lightw. Technol.*, vol. 36, no. 10, pp. 1979–1984, May 2018.
[26] J. Li, S.-T. Wu, S. Brugioni, R. Meucci, and S. Faetti, "Infrared refractive indices of liquid crystals," *J. Appl. Phys.*, vol. 97, no. 7, 2005, Art. no. 073501.
[27] B. E. A. Saleh and K. Lu, "Theory and design of the liquid crystal TV as an optical spatial phase modulator," *Opt. Eng.*, vol. 29, no. 3, pp. 240–246, 1990.
[28] S. Humbatov, M. Ramazanov, and A. İmamaliyev, "The study of BaTiO3 nanoparticles effect on threshold properties of Liquid Crystal 5CB," *Mol. Crystals Liquid Crystals*, vol. 646, no. 1, pp. 263–267, 2017.
[29] E. P. Raynes, R. J. A. Tough, and K. A. Davies, "Voltage dependence of the capacitance of a twisted nematic liquid crystal layer," *Mol. Crystals and Liquid Crystals*, vol. 56, no. 2, pp. 63–68, 2011.
[30] L. Cheng, Z. Wang, X. He, and P. Cao, "Plasmonic nanosensor based on multiple independently tunable Fano resonances," *Beilstein J. Nanotechnology*, vol. 10, pp. 2527–2537, 2019.